

“Supporting Information”

Fe-Treated Heteroatom (S/N/B/P)-Doped Graphene Electrocatalysts for Water Oxidation

Fatemeh Razmjooei, Kiran Pal Singh, Dae-Soo Yang, Wei Cui, Yun Hee Jang,* and Jong-Sung Yu*

Department of Energy Systems Engineering, DGIST, Daegu 42988, Republic of Korea

Corresponding Authors

* E-mail for J.-S. Yu: jsyu@dgist.ac.kr

* E-mail for Y. H. Jang: yhjang@dgist.ac.kr

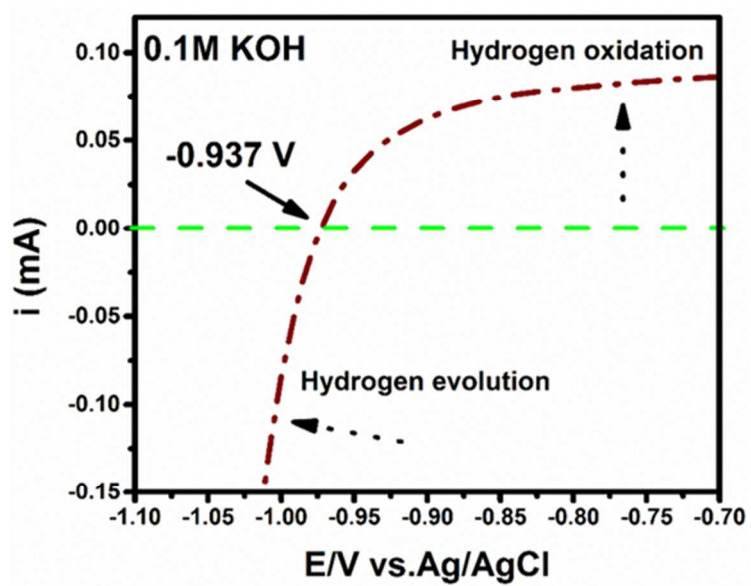


Figure S1. Calibration of the reference electrode against RHE.

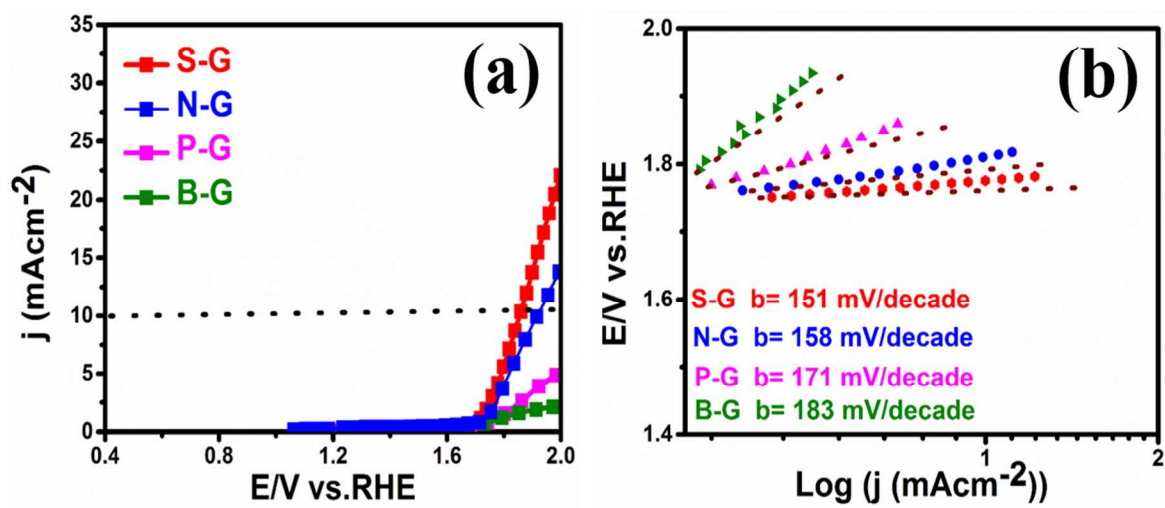


Figure S2. (a) LSV profiles and (b) Tafel plots of Fe-free catalysts, S-G, N-G, P-G, and B-G.

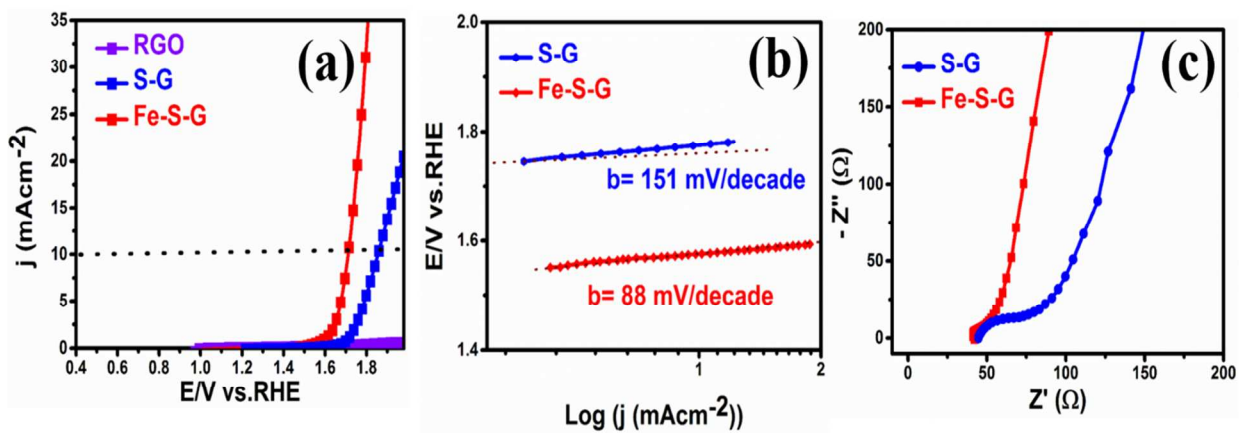


Figure S3. (a) LSV profiles of pristine RGO, S-G, and Fe-S-G, (b) Tafel plots of S-G and Fe-S-G, and (c) EIS Nyquist plots measured for S-G and Fe-S-G for OER.

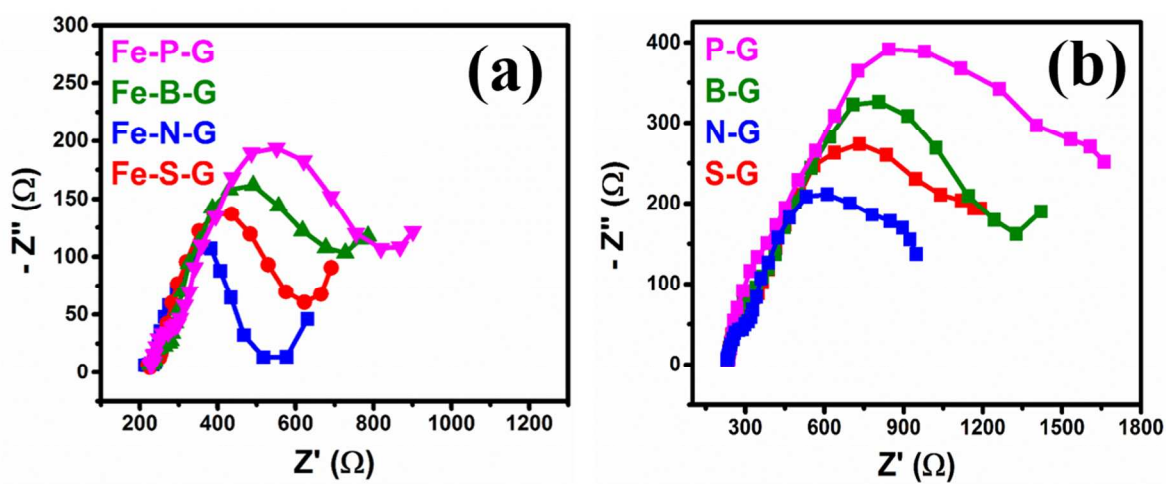


Figure S4. EIS Nyquist plots measured for (a) Fe-X-G and (b) X-G catalysts at the potential near to the onset of the OER.

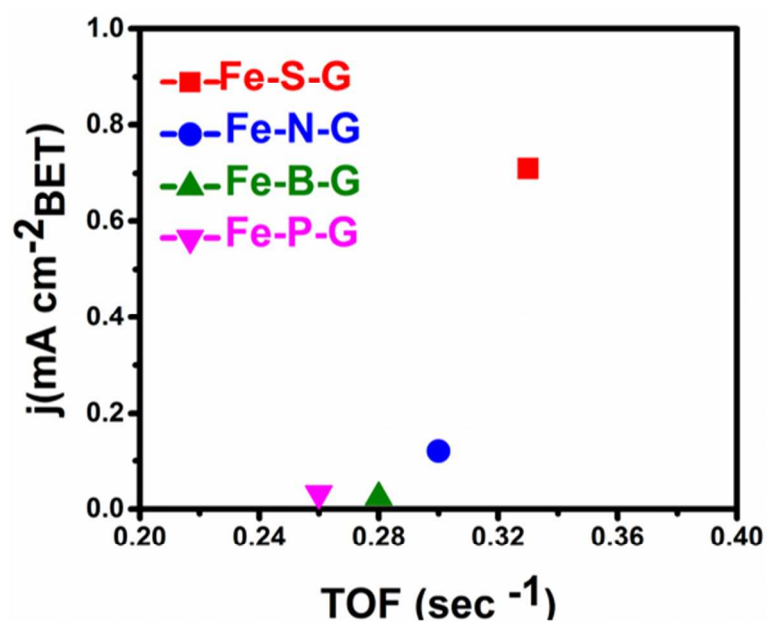


Figure S5. Comparison of turnover frequencies of Fe-X-G catalysts.

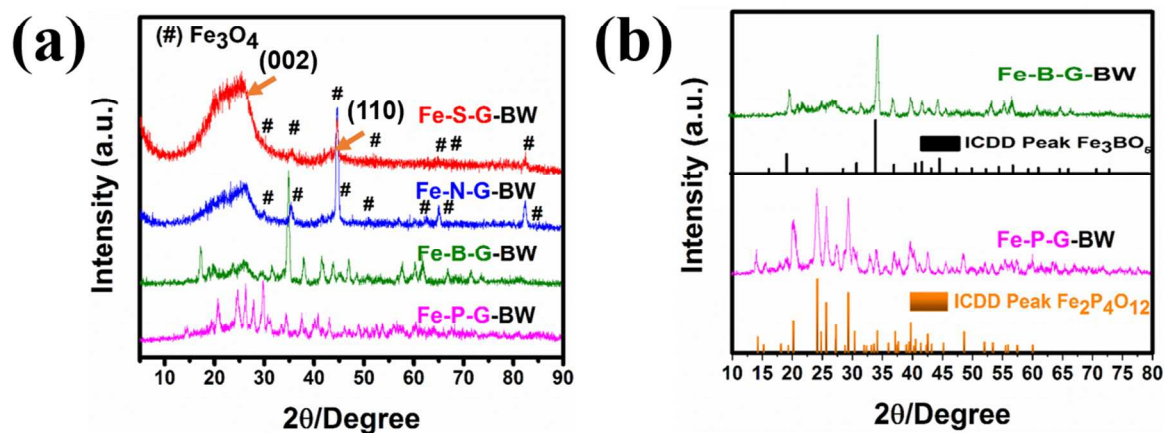


Figure S6. XRD patterns of (a) Fe-S-G, Fe-N-G, Fe-B-G, and Fe-P-G before acid washing (BW) and (b) Fe-B-G-BW and Fe-P-G-BW and ICDD reference peaks of Fe_3BO_5 and $\text{Fe}_2\text{P}_4\text{O}_{12}$ complexes, respectively, which may be present in Fe-B-G-BW and Fe-P-G-BW.

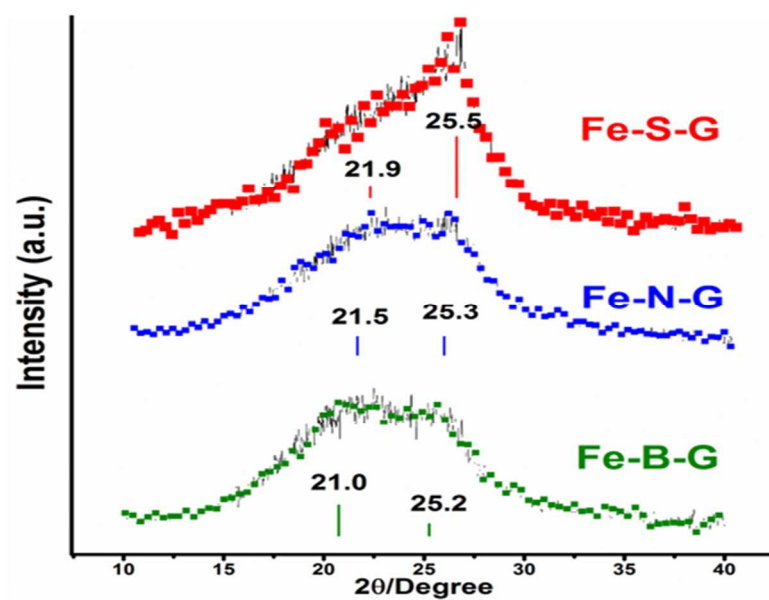


Figure S7. Magnification of XRD patterns of Fe-S-G, Fe-N-G, and Fe-B-G in the range of $2\theta = 10-40^\circ$.

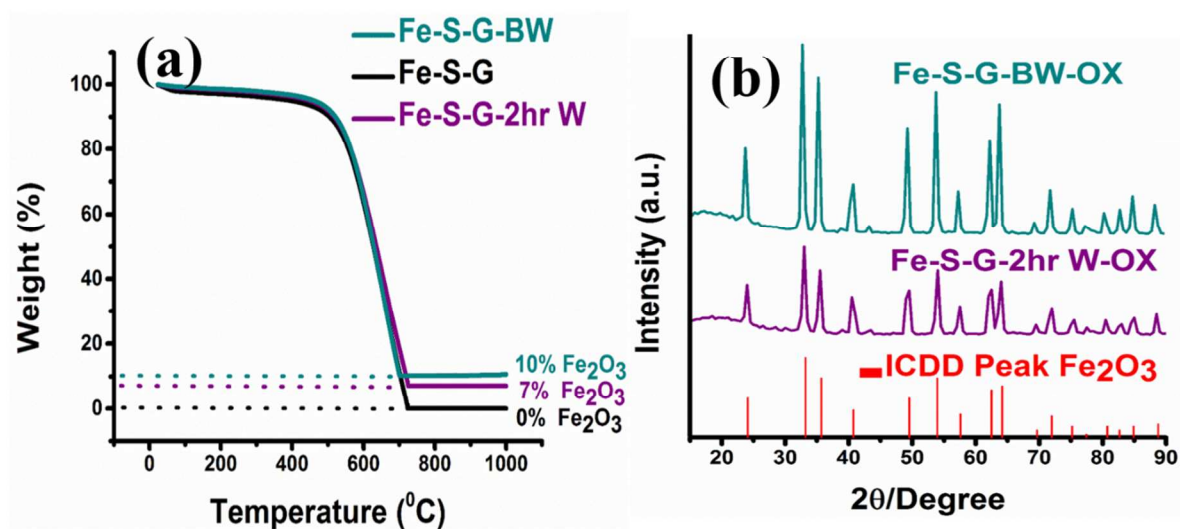


Figure S8. (a) TGA curves of Fe-S-G-BW, Fe-S-G-2hr W, and Fe-S-G measured from 25 to 1000 $^{\circ}\text{C}$ in atmospheric air. (b) XRD patterns of Fe-S-G-BW-OX and Fe-S-G-2hr W-OX, which are left over after the oxidation of Fe-S-G-BW and Fe-S-G-2hr W samples in air atmosphere along with ICDD reference peaks of Fe_2O_3 .

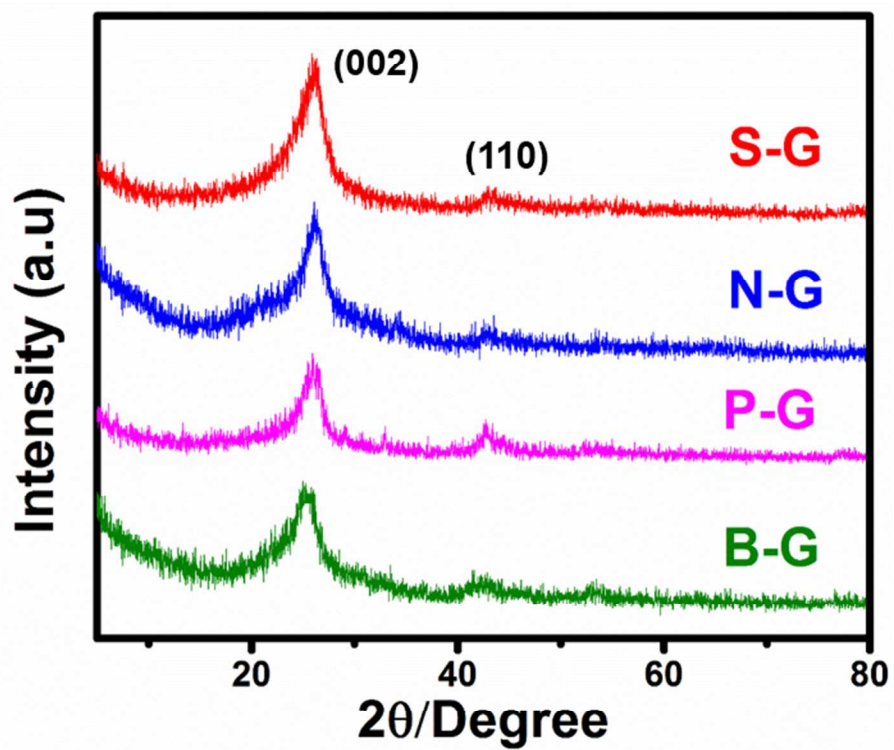


Figure S9. XRD patterns of Fe-free samples, S-G, N-G, P-G, and B-G.

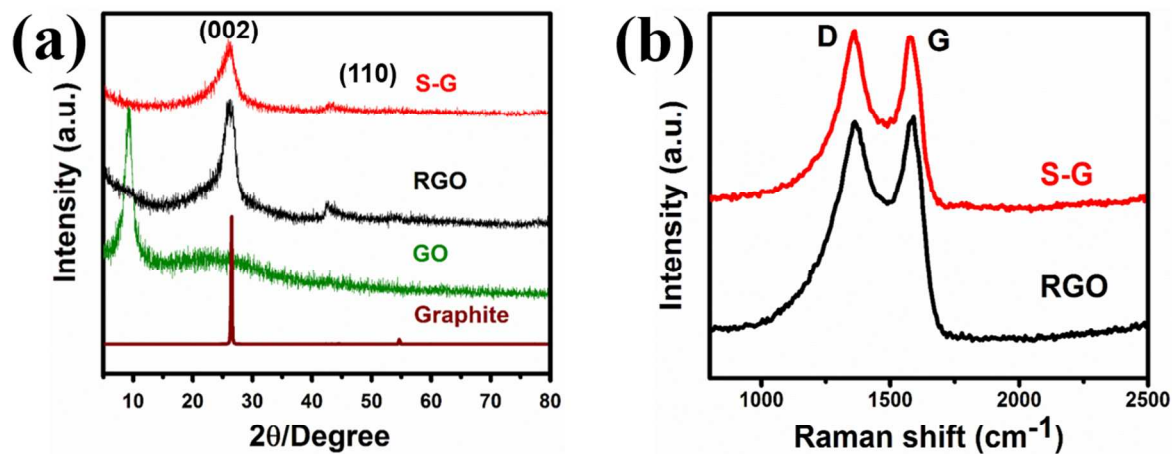


Figure S10. (a) Comparative XRD plots of graphite, GO, RGO, and S-G and (b) Raman analysis of RGO and S-G.

As shown in Figure S10a, during oxidation of graphite, oxygen functionalities intercalate between the graphene sheets, due to which the distance between graphitic layers can be increased from 3.34 to 8.3 Å, which is evident from the shifting of the (002) diffraction peak from 26.3° of graphite to 9.6° for GO.¹ After thermal reduction, the (002) diffraction peak shifts to 25-26°, which signifies the restacking of the graphene layers due to the removal of oxygen functionalities in RGO. In the same way as RGO, typical (002) diffraction peak at 26.3 and (100) peak at 43 can be seen in S-G sample. The observed peaks indicate that the S-G material is a graphite-based material. As shown in Figure S10b, the higher I_D/I_G ratio of S-G (1.12) compared to that of RGO (0.97) indicates that the disorderedness in graphitic structure increases for S-G due to the structure distortions caused by the introduction of S species into the RGO graphitic planes.

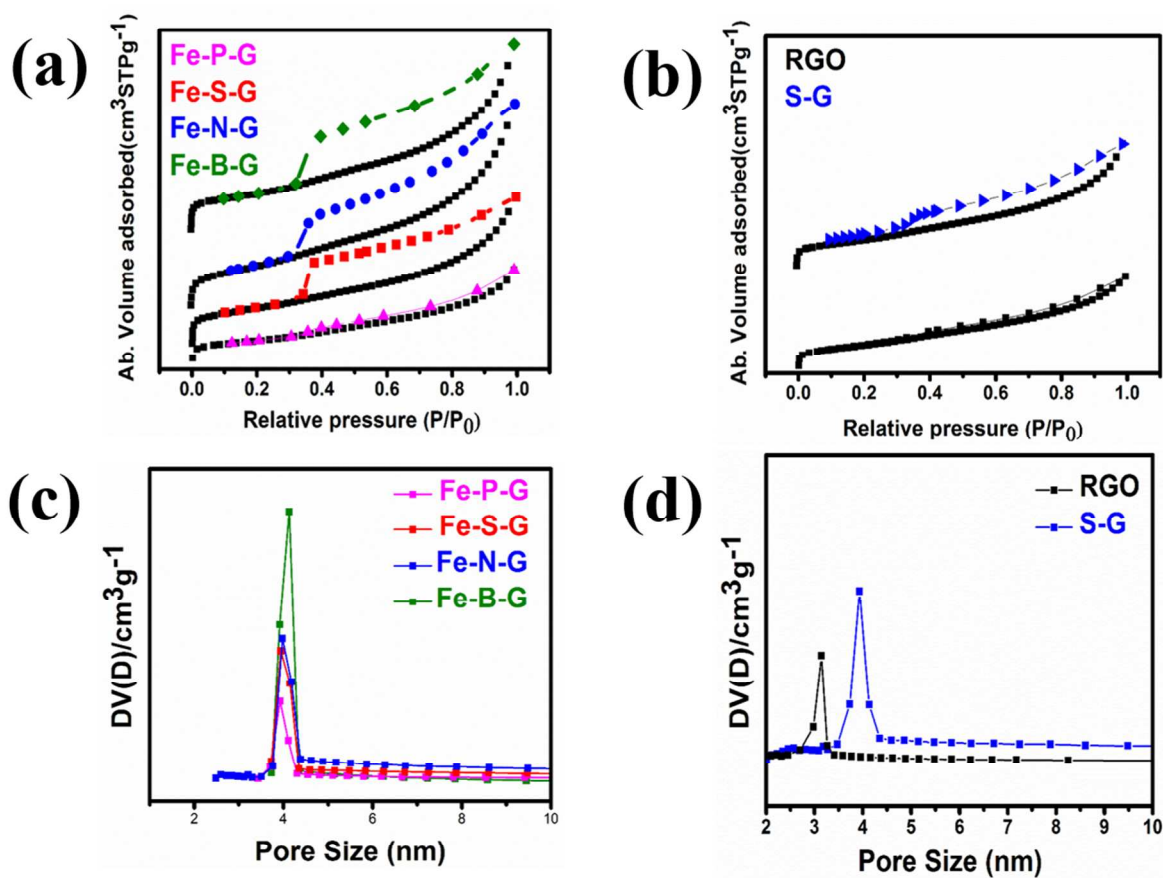


Figure S11. Nitrogen adsorption-desorption isotherms for (a) all the Fe-X-G catalysts and (b) pristine RGO and S-G. The corresponding pore size distribution curves obtained from the BJH method for (c) all the Fe-X-G catalysts and (d) pristine RGO and S-G.

Table S1 Structural characteristics by nitrogen sorption data of pristine RGO, S-G and all the Fe-treated heteroatom-doped RGOs.

Physical characteristics					
Sample	BET total surface area (m ² g ⁻¹)	Mesopore surface area (m ² g ⁻¹)	Pore volume (cm ³ g ⁻¹)	Mesopore volume (cm ³ g ⁻¹)	BJH pore size (nm)
RGO	185.12	95.61	0.18	0.14	3.11
S-G	240.10	145.13	0.30	0.22	3.95
Fe-S-G	300.81	217.96	0.45	0.40	3.98
Fe-N-G	307.58	228.88	0.51	0.45	4.01
Fe-B-G	354.36	283.37	0.57	0.53	4.12
Fe-P-G	212.24	142.98	0.27	0.16	3.93

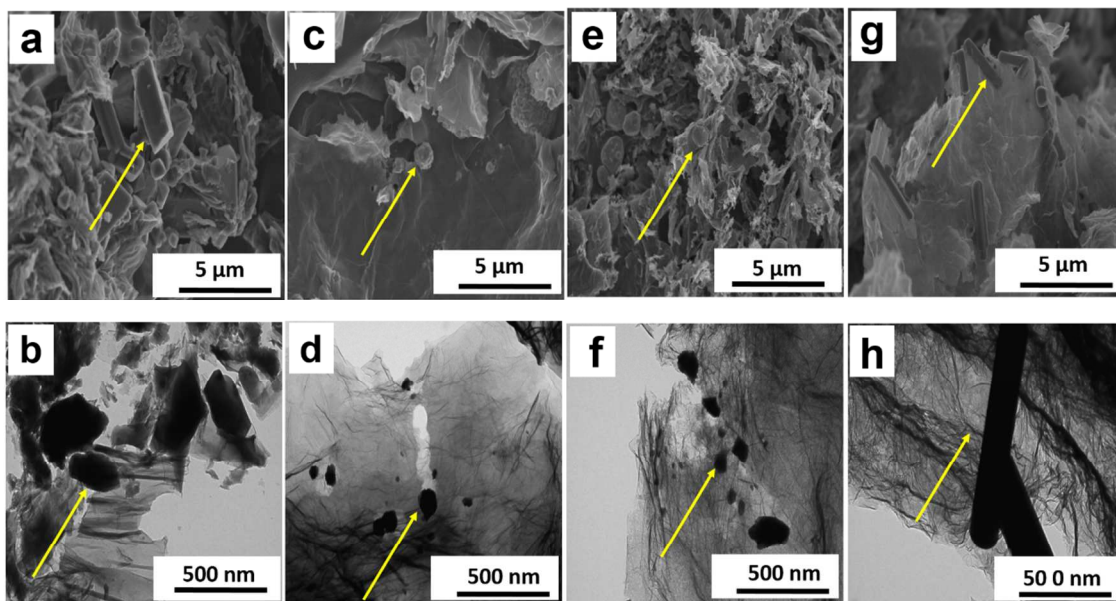


Figure S12. SEM and TEM images of Fe-P-G-BW (a and b), Fe-S-G-BW (c and d), Fe-N-G-BW (e and f), and Fe-B-G-BW (g and h).

SEM and TEM images of all the Fe-treated samples before acid washing are shown in Figure S12. Images show the presence of some small and large particles on the RGO surface formed during the annealing process. The images in Figure S12 (a and b) for Fe-P-G-BW reveal the presence of large cubic shaped particles along with other much smaller particles on the surface of RGO. These particles can be ascribed to the presence of $\text{Fe}_2\text{P}_4\text{O}_{12}$ as shown in XRD (Figure S6a). As depicted in Figure S12(c and d) and (e and f), some small particles were observed on the surface of Fe-S-G-BW and Fe-N-G-BW samples, which can be attributed to the presence of Fe_3O_4 particles, which have also been observed in the XRD patterns (Figure S6a). Figure S12 (g

and h) shows the distribution of large size rod type Fe_3BO_5 particles on RGO surface, which have already been proved by XRD (Figure S6a).

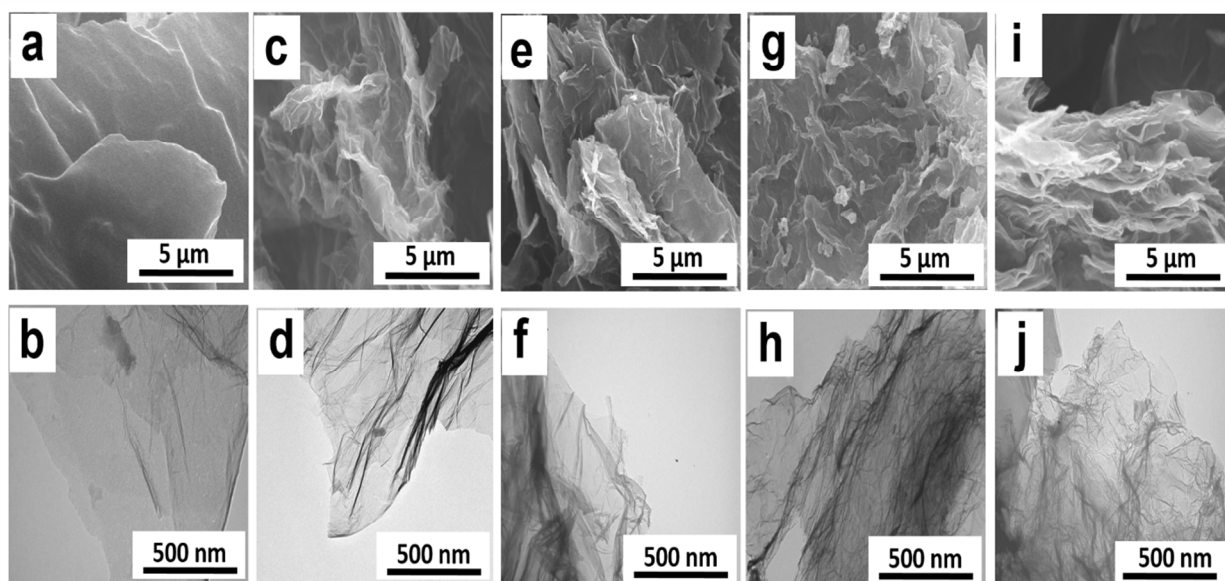


Figure S13. SEM and TEM images of pristine RGO (a and b), S-G (c and d), N-G (e and f), B-G (g and h), and P-G (i and j).

SEM and TEM images of pristine RGO and all the Fe-free samples S-G, N-G, B-G, and P-G are shown in Figure S13 (a-j). Images reveal the evolution of wrinkled patterns in heteroatom-doped RGO catalysts prepared by the thermal annealing of GO in the presence of different acid families such as sulfuric, nitric, boric, and phosphoric acids used as S, N, B, and P precursors, which can be ascribed to heteroatom doping in RGO framework. Slightly increased distortion is observed for Fe-treated heteroatom-doped RGOs compared with their Fe-free heteroatom-doped RGO counterpart catalysts. This can be due to the removal of iron species after mild acid treatment, which is present in the form of solid iron oxides formed during the annealing process as shown in Figure S6a of SI and Figure 3 in the main text.

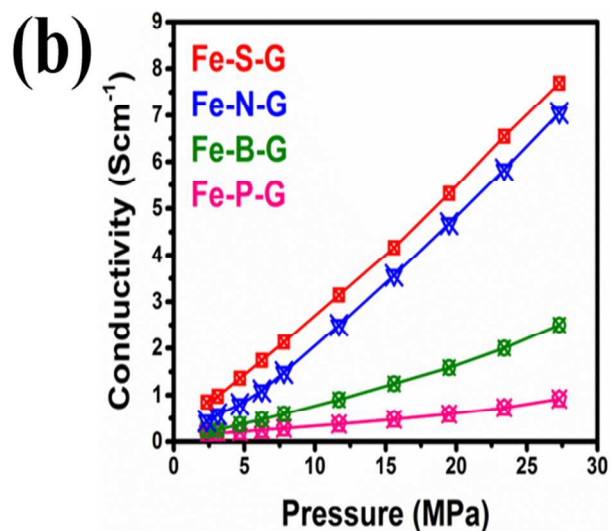
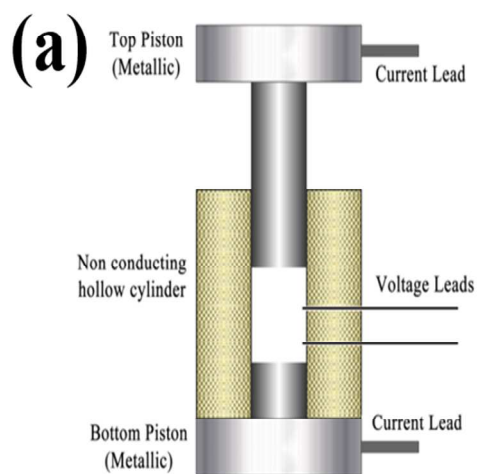


Figure S14. (a) Design of a four-probe apparatus used to measure conductivity of the powder carbon samples and (b) comparative conductivity patterns of all the Fe-treated heteroatom-doped RGOs.

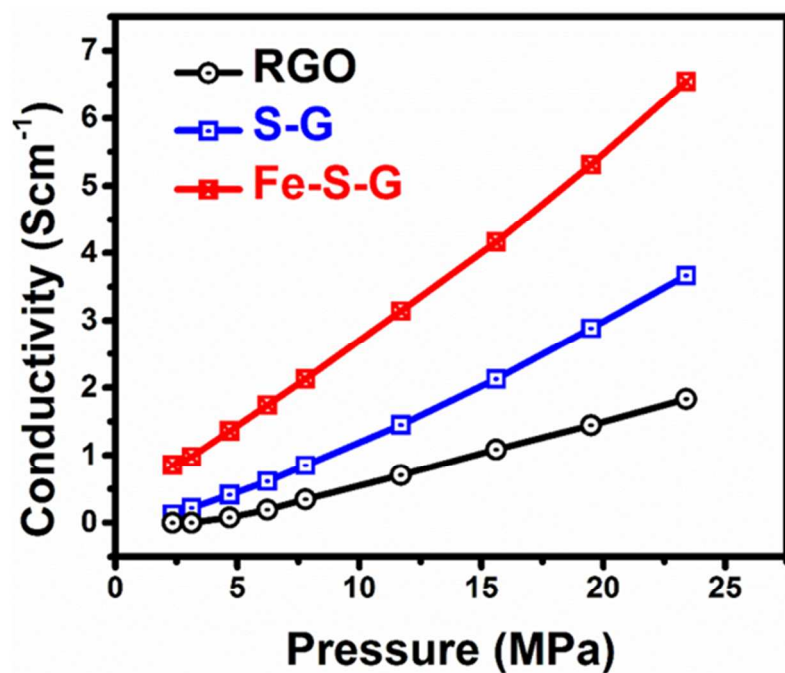


Figure S15. Conductivity patterns of the RGO, S-G, and Fe-S-G.

It is found that conductivity of Fe-S-G sample improves prominently compared with that of S-G and RGO samples. It is reported that a decrease in the amount of framework oxygen helps to increase the conductivity,² and consequently improves OER activity, which is evident from the higher C/O ratio of prepared Fe-S-G catalyst (72.8) compared with that of S-G (29.1) and RGO (27.1) (Table S2). Therefore, the Fe-S-G with lower amount of oxygen compared with that of S-G and RGO shows higher conductivity and consequently higher OER activity. This shows the role of Fe in improving the electrical conductivity and ultimately enhancing OER activity.

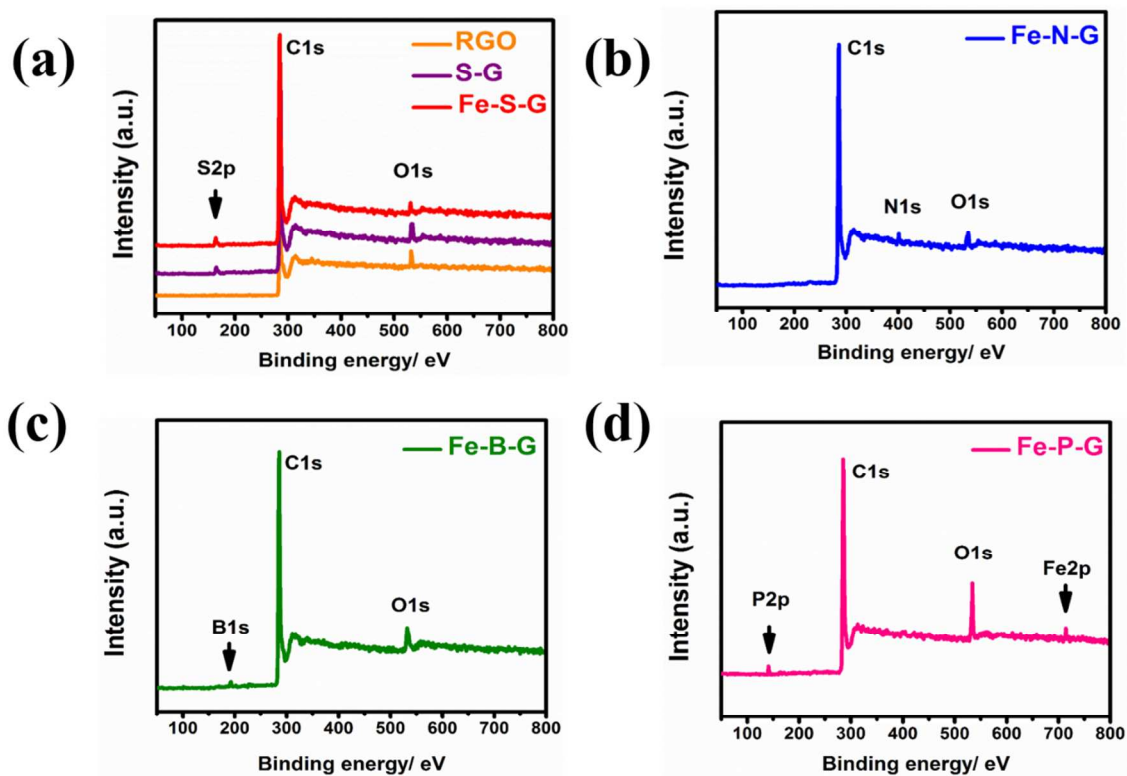


Figure S16. (a) The comparative XPS spectra of pristine RGO, S-G, and Fe-S-G and XPS spectra of (b) Fe-N-G, (c) Fe-B-G, and (d) Fe-P-G.

Table S2 Surface element contents obtained from the XPS analysis for pristine RGO and all the Fe-treated heteroatom-doped RGOs.

Sample	Atomic composition (%)						
	C 1s	O 1s	S 2P	N 1s	B 1s	P 2p	Fe2p
RGO	96.44	3.56					
Fe-S-G	96.84	1.33	1.83				-----
Fe-N-G	95.38	2.69		1.93			-----
Fe-B-G	94.88	3.61			1.51		-----
Fe-P-G	89.21	7.03				2.55	1.21

Table S3 Surface element contents obtained from the XPS analysis for all the Fe-free heteroatom-doped RGOs.

Sample	Atomic composition (%)						
	C 1s	O 1s	S 2P	N 1s	B 1s	P 2p	Fe2p
S-G	95.02	3.27	1.71				
N-G	94.12	4.03		1.85			-----
B-G	92.10	5.14			2.76		-----
P-G	93.44	4.48				2.08	-----

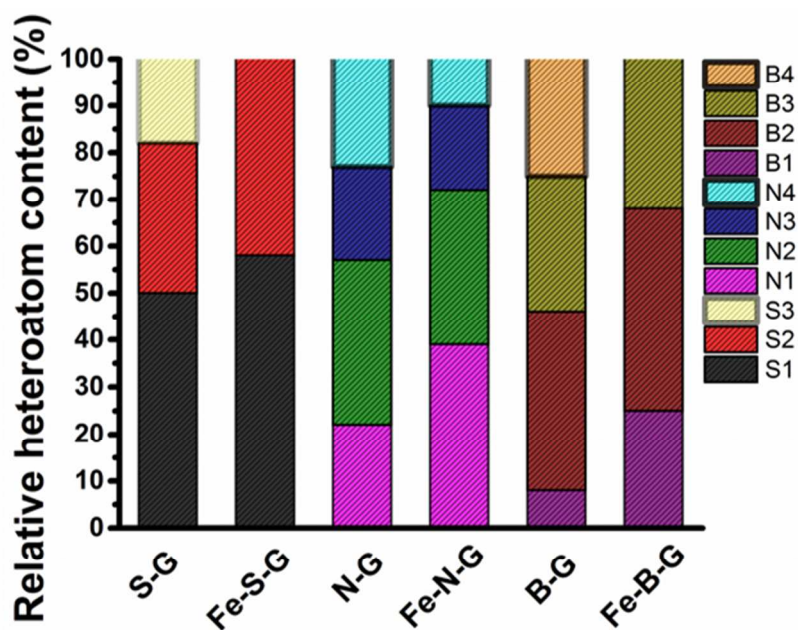


Figure S17. Relative distribution of prominent heteroatom species for Fe-S-G, Fe-N-G, and Fe-B-G catalysts and their Fe-free counterparts.

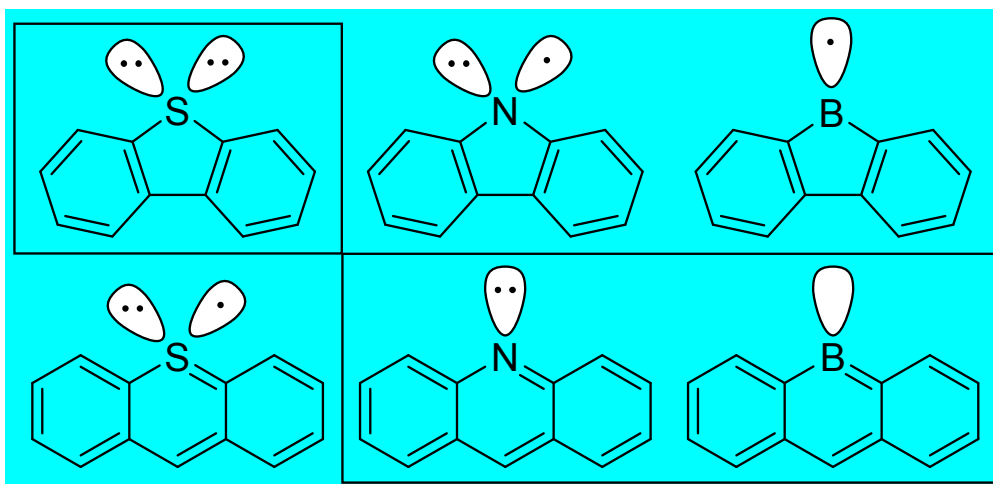


Figure S18. Electron configurations of heteroatoms ($X = \text{S}, \text{N},$ and B) in two types of molecular models for X -doped graphene edges ($X\text{-G}$): (upper) 5-membered-ring model (thiophene-S, pyrrolic-N, and 5-membered-ring model for B-G) and (lower) 6-membered-ring model (pyridinic N) in lower row. Supposedly stable models with closed-shell electronic configurations are enclosed in boxes.

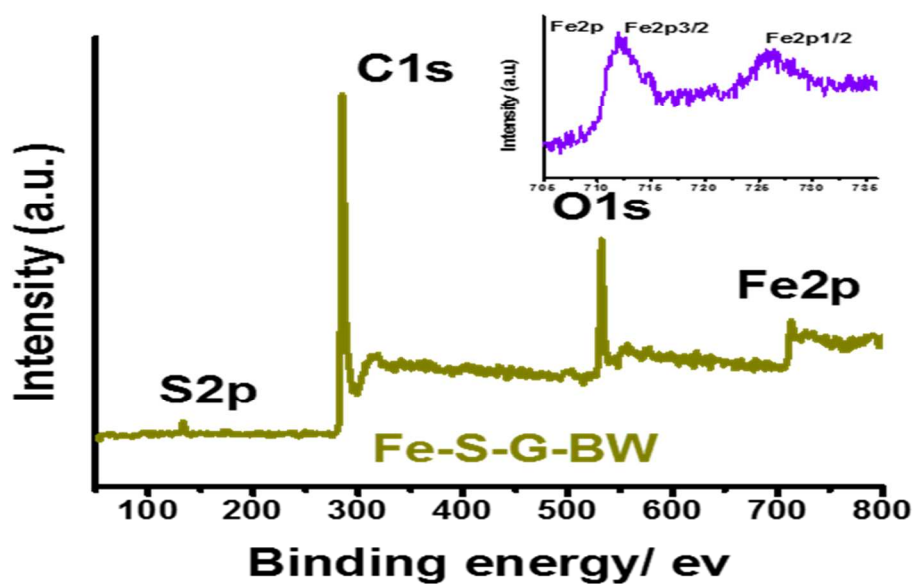


Figure S19. The XPS survey spectrum of Fe-S-G-BW. The inset is Fe 2p narrow scan spectrum of Fe-S-G-BW.

Table S4 Surface element contents obtained from the XPS analysis for Fe-S-G-BW and Fe-S-G.

Sample	Atomic composition (%)					
	C 1s	O 1s	S 2P	N 1s	B 1s	P 2p
Fe-S-G-BW	93.01	4.06	1.85			1.08
Fe-S-G	96.84	1.33	1.83			-----

Table S5 Structural characteristics by nitrogen sorption data of Fe-S-G-BW and Fe-S-G.

Physical characteristics					
Sample	BET total surface area (m^2g^{-1})	Mesopore surface area (m^2g^{-1})	Pore volume (cm^3g^{-1})	Mesopore volume (cm^3g^{-1})	BJH pore size (nm)
Fe-S-G-BW	229.12	112.34	0.28	0.19	3.44
Fe-S-G	300.81	217.96	0.45	0.40	3.98

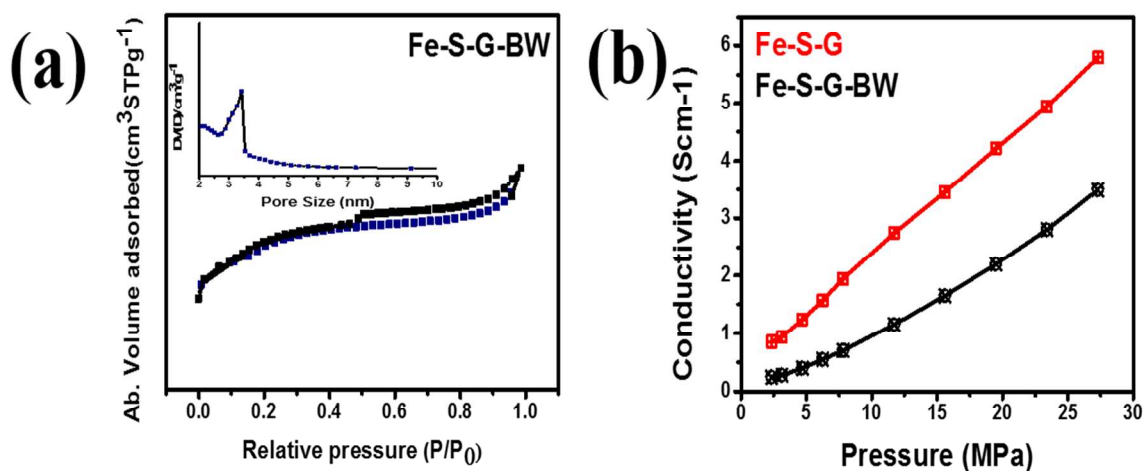


Figure S20. (a) Nitrogen adsorption-desorption isotherms of Fe-S-G-BW. The inset is the corresponding pore size distribution curve obtained from the BJH method for Fe-S-G-BW. (b) Conductivity patterns of the Fe-S-G-BW and Fe-S-G.

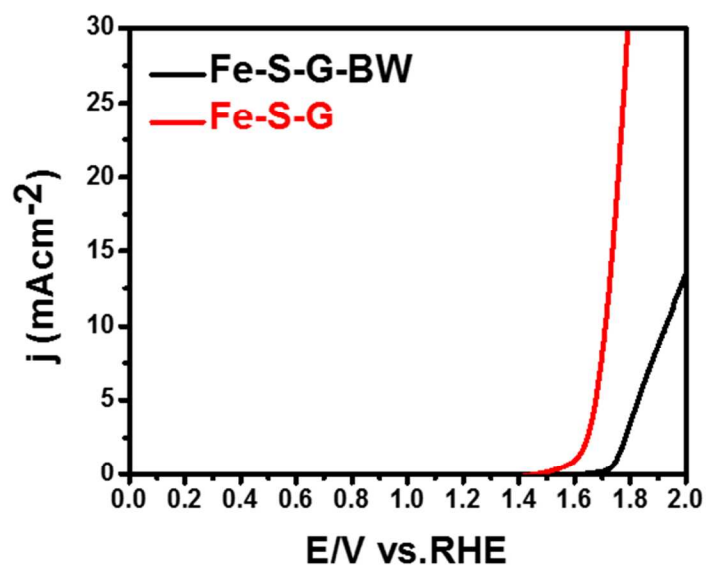


Figure S21. LSV profiles of for Fe-S-G catalyst before and after acid treatment.

REFERENCES

- (1) Razmjooei, F.; Singh, K.P.; Song, M.Y.; Yu, J.-S. *Carbon* **2014**, 78, 257-267.
- (2) Singh, K.P.; Song, M.Y.; Yu, J.-S. *J. Mater. Chem. A* **2014**, 2, 18115-18124.